JGR Space Physics

RESEARCH ARTICLE
10.1029/2019JA027160

Key Points:
- The voltage series of a riometer is accurately modeled by a stochastic process including a harmonic function expansion component
- The power spectrum estimate for the voltage series contains multiplets centered near the harmonic frequencies of one cycle per sidereal day
- Several of the detected spectral peak frequencies lie near established solar mode frequency estimates

Supporting Information:
- Supporting Information S1
- Data Set S1
- Data Set S2
- Data Set S3
- Data Set S4
- Data Set S5
- Data Set S6
- Data Set S7
- Data Set S8
- Data Set S9
- Data Set S10
- Data Set S11
- Data Set S12
- Data Set S13
- Data Set S14
- Data Set S15
- Data Set S16
- Data Set S17
- Data Set S18
- Data Set S19
- Data Set S20
- Data Set S21
- Data Set S22
- Data Set S23
- Data Set S24

Correspondence to:
F. A. Marshall,
francois.marshall@queensu.ca

Citation:
Marshall, F. A., Thomson, D. J., Chave, A. D., Fiori, R. A. D., & Danskin, D. W. (2020). A characterization of periodicity in the voltage time series of a riometer. *Journal of Geophysical Research: Space Physics*, *125*, e2019JA027160. https://doi.org/10.1029/2019JA027160

Received 15 JUL 2019
Accepted 24 MAR 2020
Accepted article online 20 APR 2020

A Characterization of Periodicity in the Voltage Time Series of a Riometer

F. A. Marshall[1], D. J. Thomson[1], A. D. Chave[2], R. A. D. Fiori[3], and D. W. Danskin[3]

[1]Department of Mathematics and Statistics, Queen's University, Kingston, Ontario, Canada, [2]Department of Applied Ocean Physics and Engineering, Woods Hole Oceanographic Institution, Woods Hole, MA, USA, [3]Geomagnetic Laboratory, Natural Resources Canada, Ottawa, Ontario, Canada

Abstract This paper reveals unprecedented periodicity in the voltage series of relative ionospheric opacity meters (riometers) of the Canadian Riometer Array (CRA). In quiet times, the riometer voltage series is accurately modeled by a stochastic process whose components include both a six term expansion in harmonic functions and some amplitude modulated modes of lower signal to noise ratio (SNR). In units of cycles per sidereal day (cpsd), the frequencies of the six harmonic functions lie within 0.01 cpsd of an integer. Earth's rotation induces a splitting of the low SNR components, resulting in the appearance of nine multiplets in standardized power spectrum estimates of the considered CRA voltage series. A second feature of these spectrum estimates is a 6 min periodic element appearing in both the CRA voltage series and the proton mass density series of the Advanced Composition Explorer (ACE). Spectral peak frequencies have been detected, which lie near established solar mode frequency estimates. In addition, some of these peak frequency estimates are coincident with peak frequency estimates of the standardized power spectra for the time series of proton mass density and interplanetary magnetic field strength (IMF) at ACE.

1. Introduction

The Canadian Space Weather Forecast Centre (CSWFC) of Natural Resources Canada (NRCan) conducts research about the space weather environment between 40° and 90° magnetic latitude for the following two purposes. The first is to achieve an improved understanding of the science of space weather, and the second is to forecast conditions for long distance radio communication. The CSWFC provides corporations and government agencies with forecasts of the atmospheric conditions for over the horizon communication. To this end, the signals of interest in the riometer studies have frequencies lying in the subinterval between 3 and 30 MHz (written as [3, 30] MHz) of the high frequency (HF) band (Fiori & Danskin, 2016). This mode of communication involves refracting or reflecting HF radio signals in the E and F regions, ionospheric layers whose respective altitude ranges are [90, 170] km and [170, 1,000] km (Prölss, 2010). In times of space weather events like solar storms, signal intermittency is maximal because of phenomena, which influence the regions between the ionospheric transport media and the transmitter and receiver stations. In particular, an enhanced influx of solar energetic particles (SEPs) mediates the attenuation of HF communication signals in the D region, itself an ionospheric layer in the [45, 100] km altitude range (Fiori & Danskin, 2016). The SEP influx raises D region ionization rates, leading to an increased frequency of collisions between electrons and heavy ions (Rogers & Honary, 2015). In these collisions, the electrons transfer all of their kinetic energy to the heavy ions in a phenomenon called absorption (Browne et al., 1995).

The riometer detection system includes an HF receiver antenna, which is oriented toward the zenith and tuned to receive in a subinterval of the [20, 60] MHz frequency band (Fiori & Danskin, 2016). The antenna system transmits signals to the riometer instrument. The riometer includes a diode component, and the diode current is balanced with the input antenna signal to achieve an equal noise power. Subsequently, the balanced diode current is converted to a voltage response (Little & Leinbach, 1959). In riometer studies, the quantity of interest is called the absorption variable, a height integrated attenuation rate for those radio waves, which propagate in the vertical axis of the receiver antenna (Rogers & Honary, 2015). The absorption variable is so named because it quantifies the degree of D region radio wave absorption. It is measured in units of decibels, and absorption values are inferred from the time series of riometer voltage. In addition, the absorption variable is positively correlated with HF signal attenuation, and so it serves as a proxy for

the latter quantity. The absorption value peaks during solar storms, while falling to baseline levels in quiet times. The problem of forecasting atmospheric conditions for long range communication involves accurately detecting and characterizing absorption events, time intervals in which the absorption value exceeds 1 dB (Fiori & Danskin, 2016; Foppiano & Bradley, 1985; Hargreaves, 2010). During solar storms, different types of absorption occur, with each type characterized by both the duration of the absorption event and the geographic location of the station, which underlies the affected ionospheric area. For instance, consider the examples below from Fiori and Danskin (2016).

- Two hour shortwave fadeout events predominantly affect the dayside D region.
- Lasting up to several hours, auroral absorption events predominantly affect the nightside D region.
- Lasting up to several days, polar cap absorption events predominantly affect the nightside D region.

The above examples motivate absorption monitoring over a fraction of the northern hemisphere. To this end, NRCan and the University of Calgary jointly operate the Canadian Riometer Array (CRA) (Danskin et al., 2008), a large scale monitoring system that is sensitive to substorm events on continental and planetary scales (Spanswick et al., 2009).

The absorption value is inferred from the riometer voltage using the cosmic noise method. With the knowledge from Jansky (1933) that 20 MHz cosmic radio noise influences the ionosphere, Little and Leinbach (1959) anticipated that the voltage series could be modeled by a periodic element whose frequency is 1 cpsd. In quiet times, chromospheric, Lyman alpha emissions ionize the dayside D region, inducing positive absorption values (Laštovička, 1976). The positive absorption values are said to correspond to the phenomenon of baseline absorption. Because dayside baseline absorption values systematically exceed nightside baseline absorption values, it might be expected that the voltage series is accurately modeled by a second periodic element of frequency equal to one cycle per mean solar day (1 cpmsd).

This paper reveals that some periodic elements in the riometer voltage may well arise from a coupling between this voltage and solar modes. Motivating this hypothesis, the following examples illustrate how observations of unexpected coupling between geophysical and resonant phenomena are precedented.

- The rotation of Earth's core mantle boundary influences tides (Agnew, 2019).
- During the testing of nuclear weapons, infrasound bursts yield waves that couple with atmospheric processes (de Groot Hedlin, 2016).
- In quiet times, the solar wind pressure influences wave particle dynamics of the inner magnetosphere (Kim et al., 2018).

Consistent with the above examples, significant evidence has accumulated that solar modes influence both geophysical phenomena like oceanic and seismic velocity processes (Baker et al., 2003, 2018a, 2018b, 2019; Thomson & Vernon, 2015) and space physics parameters like particle mass density and interplanetary magnetic field (IMF Haley, 2014; Isserstedt & Schlosser, 1975; Somerset, 2017; Steffens & Nuernberger, 1998; Thomson, 2012; Thomson & Haley, 2014; Thomson et al., 1995, 2000; Thomson, Lanzerotti, Maclennan, Heber, et al., 2001; Thomson, Lanzerotti, & Maclennan, 2001, 2007).

Reviews on the subject of solar modes are included in Christensen Dalsgaard (2002), Gough and Toomre (1992), Thompson (2005), and Thomson et al. (2007). In the time series of photospheric radial velocity, spectral peaks appear that are reminiscent of those for driven, underdamped, standing waves (Chaplin et al., 1998, 2001, 2004; Claverie et al., 1979; Deubner, 2002; Gough et al., 1988; Haley, 2014; Hill et al., 1975; Korzennik et al., 2013; Stein & Leibacher, 1974; Ulrich & Rhodes Jr. 1977). Corresponding to these waves are the free oscillator solutions that would be obtained in the absence of forcing and damping (Thornton & Marion, 2004). These free oscillation solutions are modeled as the harmonic temporal factors of a spherical harmonic expansion. The terms of this expansion are called solar normal modes (Chaplin et al., 1998; Christensen Dalsgaard, 2002; Kosovichev et al., 1997). Solar modes are classified by the following taxonomy (Thomson & Vernon, 2015; Thomson et al., 2007).

- Pressure modes (p modes), which are acoustic standing waves (Christensen Dalsgaard, 2002).
- Gravity modes (g modes), characterized by a buoyancy restoring force (Berthomieu & Provost, 1991; Provost et al., 2000; Tassoul, 1980).
- Fundamental modes (f modes), which are analogous to surface gravity waves in the ocean (Gough, 1980).

A solar mode is characterized by the radial, latitudinal, and azimuthal angular momentum numbers, n, l, and m, respectively. Only p modes are considered in this paper. For this class of modes, the $|n, l$ states arise from the governing wave equation in Christensen Dalsgaard (2002) because of the assumption of spherical symmetry in the standard solar model. Any form of azimuthal asymmetry (e.g., effects induced by solar rotation or by the solar magnetic field) increases the fine structure, with the $|n, l$ states expressed as linear combinations of $|n, l, m$ states (Christensen Dalsgaard, 2002).

Models have been proposed, which convincingly demonstrate how solar modes can propagate from the photosphere to terrestrial phenomena. Consider the following examples.

- The model of Erdélyi (2005) predicts a coupling between p modes and the lower solar atmosphere.
- Those particle jet sources that are inclined, photospheric, magnetic flux tubes mediate the transfer of p mode energy from the photosphere to the chromosphere and corona (Buttighoffer et al., 1999; de Pontieu et al., 2005; Fisk, 1995, 1996; Schwenn, 2007; Thomson et al., 2007).
- Ghosh et al. (2009) demonstrates how Alfvén waves can propagate from the photosphere to Earth's bow shock, carrying with them a solar mode signature.
- Thomson and Vernon (2015) speculates that Alfvén waves transport solar modes from the magnetosphere to phenomena further in toward Earth's surface.

2. Techniques for Detecting Amplitude Modulated Solar Modes

In this paper, $\mathbb{Z}$ denotes the set of all integers, $\mathbb{N}$ the set of all positive integers, and Δt the sampling period of a time series. In addition, K denotes the number of taper sequences used in the multitaper spectral analysis. The mth frequency in the grid of the fast Fourier transform (FFT) is denoted by f_m. What now follows is a description of the stochastic process used to model all of the time series considered for analysis in this paper. Denote by $\mathbf{x}$ a time series, where $\mathbf{x}^{\mathrm{T}} = [x_n]_{n=0}^{N-1}$ and where x_n is the nth time series measurement. The time series is modeled by the random vector, $\mathbf{X}$, where $\mathbf{x}^{\mathrm{T}} = [x_n]_{n=0}^{N-1}$. The components of $\mathbf{X}$ are defined as time elements of the discrete time, stochastic process, $\mathbb{X}$, with $\mathbb{X} = \{X_n\}_{n\in\mathbb{Z}}$. Here, X_n denotes a time element, $X_n = X(n\Delta t)$, from the continuous time, stochastic process, X. The importance of specifying X is that the proposed time series model is applicable for any N and any Δt.

The discrete time process is represented by

$$\mathbb{X} = \mathbb{x}^{(HS)} + \mathbb{x}^{(MS)} + \mathbb{X}^{(RES)}, \tag{1}$$

where HS and MS respectively stand for high and medium signal to noise ratio (SNR). The $\mathbb{x}^{(HS)}$ high SNR component is defined by $\mathbb{x}^{(HS)} = \left\{x_n^{(HS)}\right\}_{n\in\mathbb{Z}}$, with

$$x_n^{(HS)} \overset{m.s.}{=} \sum_{l\in\mathbb{N}} x^{(HS,l)} \exp\left(i2\pi f^{(HS,l)} n\right). \tag{2}$$

Here, the equality, $\overset{m.s.}{=}$, is said to be in the mean square limit in the sense of section 2.8 in Brockwell and Davis (1991). The $x^{(HS,l)}$ and the $f^{(HS,l)}$ respectively denote nonrandom amplitudes and frequencies.

In equation (1), the $\mathbb{x}^{(MS)}$ medium SNR component is defined analogously to $\mathbb{x}^{(HS)}$. The terms in the two expansion representations of $\mathbb{x}^{(HS)}$ and $\mathbb{x}^{(MS)}$ are said to comprise the harmonic components of $\mathbb{X}$. The lth high SNR harmonic component yields a $> 99.9\%$ significant peak in the spectrum of multitaper harmonic Fisher statistic values (SNR estimates), where significance is determined by the $F_{2,2K-2}$ distribution of the frequency $f^{(HS,l)}$ Fisher statistic under the null hypothesis of $x^{(HS,l)} = 0$. For further details regarding the multitaper harmonic Fisher test, refer to Fisher (1939), Snedecor (1938), and Thomson (1982). The lth medium SNR harmonic component is defined analogously to the lth high SNR harmonic component, with the exception that now the >99.9% significant peak is in the spectrum of residual multitaper harmonic Fisher statistic values. The significance is determined by the $F_{2,2K-5}$ distribution of the frequency $f^{(MS,l)}$ residual multitaper harmonic Fisher statistic under the null hypothesis of $x^{(MS,l)} = 0$. For details regarding the residual multitaper harmonic Fisher test, refer to section 5 in Thomson (1990).

The zero mean residual component, $\mathbb{X}^{(RES)}$, is represented by $\mathbb{X}^{(RES)} = \mathbb{X}^{(LIN)} + \mathbb{X}^{(NL)}$, where $\mathbb{X}^{(LIN)}$ is the output of a causal, autoregressive (AR) filter whose input is the nonlinear process, $\mathbb{X}^{(NL)}$. The nonlinear component

is represented by $\mathbb{X}^{(NL)} = \mathbb{x}^{(LS)} + \mathbb{X}^{(PE)}$. The harmonizable, locally white, prediction error component, $\mathbb{X}^{(PE)}$, satisfies the following condition on $\mathbf{X}^{(PE)}$, where $\left(\mathbf{X}^{(PE)}\right)^{\mathrm{T}} = \left[X_n^{(PE)}\right]_{n=0}^{N-1}$. At the frequency, f_m, the K multitaper discrete Fourier transform (DFT) transformations of $\mathbf{X}^{(PE)}$ are independent and identically distributed as an asymptotically complex Gaussian random variable as N approaches infinity. This last assumption is motivated by the following references.

- The theory in Andrews (1983), Brillinger (1981), Brockwell and Davis (1991), Granger (1976), Hannan (1970), Mallows (1967), and Rosenblatt (1961).
- The empirical evidence in Haley (2014), Marshall and Thomson (2017), Marshall et al. (2018), Thomson (1990), Thomson and Chave (1991), Thomson et al. (2001), Thomson (2007), and Thomson and Haley (2014).

A consequence of the harmonizability assumption above is that each of the $X_n^{(PE)}$ is represented by the mean square limit of a sequence of harmonic function expansions, where the expansion coefficients are random (Loève, 1960). The terms of one element of this sequence are said to be spectral components of $\mathbb{X}^{(PE)}$. It follows from the model design for $\mathbb{X}$ that this process is also defined by a collection of spectral components.

The low SNR component, $\mathbb{X}^{(LS)}$, satisfies (equation (8) in Thomson et al., 2001)

$$x_n^{(LS)} \overset{m.s.}{=} \sum_{j\in\mathbb{N}} h_n^{(j)} \sum_{h\in\mathbb{N}} x^{(LS,jh)} \exp\left(i2\pi f^{(LS,jh)} n\right). \tag{3}$$

The $x^{(LS,jh)}$ are nonrandom coefficients for the harmonic expansion associated with the jth modulating sequence, $\mathbb{h}^{(j)}$, where $\mathbb{h}^{(j)} = \left\{h_n^{(j)}\right\}_{j\in\mathbb{Z}}$ and where the sequence has unit spectral energy. The $f^{(LS,jh)}$ are the nonrandom resonant frequencies defined by a wave equation for driven, underdamped oscillators. Appendix A describes the detector for low SNR components. The spectrum of test statistics will be referred to as the standardized statistic spectrum, while the spectrum of test statistic values given the data will simply be called the standardized spectrum. The (j,h)th low SNR component yields a >95% significant peak in the standardized spectrum, where significance is determined by the χ^2_{2K} distribution of the frequency $f^{(LS,jh)}$ test statistic under the null hypothesis of $x^{(LS,jh)} = 0$. As will be discussed in section 3, three time series corresponding to the three space components of the IMF strength vector from the ACE spacecraft were considered for analysis. For each of these time series, a standardized spectrum was computed. At each frequency in the FFT grid, the maximum value of the three test statistics was retained, and the resulting maximum spectrum is referred to as an IMF strength standardized spectrum.

The following novel detection scheme for amplitude modulated solar modes in the considered space physics time series of this paper is inspired by the schemes in Thomson et al. (1995) and Thomson and Vernon (2015).

Ⓐ Search each CRA standardized spectrum for frequency bands containing outstanding peaks. Peak power should achieve >95% level of the χ^2_{2K} distribution, while the peak bandwidths should lie well below 10μHz. Keep a record of spectral peak frequencies found coincident to within 4μHz in the different CRA standardized spectra.

Ⓑ For the three time series of IMF strength and for the time series of proton mass density measured at ACE and considered in section 3 for the same time window of the CRA voltage series, search the standardized spectrum for frequency bands containing outstanding peaks, as in Step A for the case of the CRA series. Keep a record of the spectral peak frequencies found coincident in the ACE and CRA standardized spectra.

Ⓒ Scan reference tables for p mode frequency estimates within 4μHz of some of the peak frequencies recorded in Steps A and B. Keep a record of these frequencies.

Ⓓ Consider the p mode reference frequency estimate was recorded in Step C and whose angular momentum state is $|n,l,m\rangle$. For the recorded frequencies in Steps A and B, search for those frequencies that satisfy the following two conditions.

- The frequency lies within 4μHz of a reference p mode frequency recorded in Step C.
- The angular momentum state of the reference p mode just mentioned is $|n',l',m'\rangle$, where $n' = n$ and either $l \neq l$ or $m' \neq m$, or both.

Keep a record of the matched frequency estimates.

Table 1
Geographic Locations of the CRA Stations Considered in This Paper

Station	OTT	BRD	MEA	INU	RES
° N	45.4	49.9	54.6	68.3	74.7
° E	284.5	260.1	246.7	226.5	265.1

Note. The acronyms are defined in the Acronyms section.

Ⓔ For the frequencies recorded in Steps A–D, search for coincidences in one or both of the following types of standardized spectra.

- Standardized spectra for different geophysical and space physics time series covering the same time window as that of the CRA series.
- Standardized spectra already discussed in this detection scheme but for different time windows to that of the CRA series.

Appendix B discusses the strengths and weaknesses of the above detection scheme. For some of the steps, the reason for choosing a 4 μHz bandwidth when assessing agreement is that this is the scale defined for the record sizes of the considered time series in this paper by the peak frequency standard deviation estimate arising from the estimator in the last equation of section 5.2 in Thomson (2000). For Step E, section 1 provides references that present evidence for a coupling between solar modes and phenomena associated with geophysical and space physics time series.

3. Data Preparation and the Calculations for Multitaper Spectral Analysis

For Step A of the detection scheme in section 2, Table 1 displays geographic locations of the CRA stations whose voltage time series were considered for analysis. The table values have been acquired from NRCan (2019). The considered riometers have low enough variability over the first 54 days of 2011 that their standardized spectra reveal a considerable number of resolved peaks. A number of riometers in the CRA like those of Penticton and Saskatoon were not selected because their high variability precludes the conspicuous appearance of such peaks (further details about the effects of the time series variability on the standardized spectrum are discussed in section 4.2.1). Southern CRA riometers were considered from the Meanook (MEA), Brandon (BRD), and Ottawa (OTT) riometers. The OTT, BRD, and MEA stations are situated outside the auroral zone, and so it was anticipated that the periodicities of these voltage series would be similar. The Inuvik (INU) station is situated in the auroral zone. For the polar cap, the Resolute (RES) voltage series was considered. It was anticipated that the periodicities of voltage series from the INU and RES riometers would differ significantly from those of the southern CRA series because of the different fields of view of the riometers and the different inclinations of geomagnetic field lines at ground level.

Based on a visual inspection of the five considered CRA voltage series, it was anticipated that the OTT voltage series would provide the most convincing detections of low SNR components because it has the greatest degree of stationarity during the first 54 days of 2011. While a longer record length might improve spectral resolution, this length was not increased because, over the course of 54 days, the p mode frequencies can shift by significant amounts on the 2 μHz scale. As long as solar activity during the 54 day time window is comparable with that in the example of section IX of Thomson et al. (2007), the frequency shift could induce significant peak broadening in the standardizes spectrum. An average flux of 88.6 solar flux units (SFU) was computed from that 1 day sampled time series of local noon solar flux from NOAA (2018), which runs from 2 January through 23 February in the year of 2011 (the value for 1 January was missing in the data set). The standard deviation for this time series is equal to 11.1 SFU. The corresponding estimates for the mean and standard deviation presented in section IX of Thomson and Vernon (2015) for the data set of NOAA (2018) between 1947 and 2004 are 119.3 and 50.2 SFU, respectively. The standardized difference between the aforementioned average estimates is 0.6, so the agreement between the flux estimates cannot be ruled out at the 95% level under the assumption of a Gaussian distribution.

For Step B, the ACE time series considered for analysis included the X, Y, and Z IMF strength series from the Magnetic Field Experiment (MAG) instrument (ACE/MAG Project, 2008) and the proton mass density series from the Solar Wind Electron, Proton and Alpha Monitor (SWEPAM) (Smith & L'Heureux, 2003). The

SWEPAM instrument records five proton density series, one for each of five energy gates in [0.047, 1.900] GeV. The proton density series associated with the [0.795, 1.193] MeV energy gate was considered for analysis because it contains remarkable features like a 2.704 mHz peak coincident with the central frequency of a multiplet common to the CRA standardized spectra (refer to section 4.2.4). The other energy gates were not considered, although they might well contain further information about the origin of the voltage periodicity.

For Step C, the following sets of reference p mode frequency estimates were considered.

1. The theoretical estimates in Table 2 of Provost et al. (2000).
2. A set of estimates derived from the entries in Tables 2 and 3 of Broomhall et al. (2009). These two tables include estimates that were computed when the measured 10.7 cm solar flux was equal to 118 and 64 SFU, respectively. The frequencies associated with the 88.6 SFU average were estimated using two point linear interpolation.

Estimates of Broomhall et al. (2009) are for the frequencies of low l p modes. These modes affect a greater number of space physics phenomena between the Sun and Earth's bow shock than the high l p modes, a result that arises from the increased spatial coverage of the photosphere by these modes.

Appendix D discusses all of the data processing and multitaper calculations for each of the time series considered in this paper. All of the time series were cleaned of outliers and decimated from 1 to 120 s sampling period, the decimation step making feasible the taper computations of the R `multitaper` library (Rahim & Burr, 2017). In calculations for the standardized spectrum, the multitaper time bandwidth parameter was set equal to 5, and the number of tapers was set to $K = 9$. For each of the considered ACE and CRA time series, this parameterization yields a multitaper spectral bandwidth of 2.1μHz. Zero padding was applied in such a way that the FFT frequency grid has 64 nHz spacing. The methods of Thomson et al. (2001) were used to compute the standardized spectrum. In particular, a third order AR prewhitener was applied, followed by a second whitening step.

4. Detected Periodic Elements in the Riometer Voltage

4.1. Summary Statistics and the Detected Harmonic Components

In this section, both the time series, $\mathbf{x}$, and all components of the time series model from section 2 will correspond to the OTT voltage series. While the signal elements of the model process, $\mathbb{X}$, cause the variance of the process element, X_n, to depend on n, each component process of $\mathbb{X}$ can nonetheless be estimated by a low order AR process (for convincing motivation, refer to the second paragraph in Example 6.1.1 of Brockwell and Davis (2002), where the considered time series is accurately modeled by both an AR process and an AR, integrated moving average process). Therefore, an average over the FFT frequency grid of multitaper spectral power estimates is an estimate of the common variance of the X_n (the variance estimator is defined in the last of the equations in Thomson (1982) preceding equation (5.2)). The variance estimate for X_n is 19.0V^2. Given a 4.3 V multitaper mean estimate (refer to Burr, 2012, for details about multitaper moment estimation), the variance estimate for $X_n - 4.3\text{V}$ is 0.65V^2 (over 3% the variance estimate for X_n). Summary statistics for the other four considered CRA series are comparable.

Table 2 displays summary statistics for the harmonic components of $\mathbb{X}$. Here, the estimate for the sidereal day period estimate is from Edgar (2018). Recall from section 2 how detections of the high and medium SNR components are made using the 99.9% threshold of the multitaper and residual multitaper harmonic Fisher tests. The second and third columns contain FFT frequencies whose multitaper harmonic Fisher statistic values achieve the global maximum of all values in a spectral peak. In the sixth column, the standard deviation estimates for the peak frequencies are obtained from the standard deviation estimator discussed in the final paragraph of section 2. The SNR estimates of the seventh column are values of the multitaper and residual multitaper Fisher statistics. These are to be compared with quantiles of the $F_{2,16}$ and $F_{2,13}$ distributions to assess the degree of statistical significance, and they are listed instead of the percentile estimates themselves because they are easier to distinguish. Two of the higher order 1 cpsd harmonic components that are not included in Table 2 are discussed in section 4.2.3. For the other four considered CRA voltage series, the results corresponding to those in Table 2 are similar.

Some of the harmonic components have been omitted from the table because they were not found coincident in all of the other CRA Fisher statistic spectra. Table 2 reveals that the most stable signal element of $\mathbb{X}^{(HS)}$ is accurately explained by a six term expansion in harmonic functions, where the harmonic components have the following frequencies:

Table 2
Statistics for the Harmonic Components of a Cleaned, Decimated Voltage Time Series Recorded by the Riometer at the OTT Station of the CRA

Frequency (±32nHz)			Relative difference (%)		Standard deviation	SNR
cpsd Rounded	cpsd	cpmsd	cpsd	cpmsd	10^{-3}cpsd	×10
1	1.0025	1.0052	0.5	1.1	3.5	15.4
1 (1)	0.9915	0.9943	0.4	0.3	15.5	
2	1.9995	2.0050	0.8	8.6	0.4	257.7
2 (1)	1.9831	1.9885	0.2	0.1	74.6	
3	3.0020	3.0103	1.3	6.7	1.1	16.4
4	3.9991	4.0100	0.4	3.9	1.9	
5	5.0016	5.0153	0.8	7.5	1.5	3.3
5 (1)	4.9468	4.9603	4.5	3.4	8.7	
8	7.9926	8.0145	3.9	7.7	1.4	1.5

Note. The time window covers the first 54 days of 2011, and the voltage series has been decimated from 1 to 120 s sampling after cleaning. The first column contains rounded values of the frequency estimates in the second column in cpsd units. In this column, the "(1)" entries specify that the detections are significant at the 99.9% level of the residual multitaper, harmonic Fisher statistic spectrum. In all rows of this column without a "(1)", the detections have been made at the 99.9% of the multitaper harmonic Fisher statistic spectrum. The second and third columns display the peak frequency estimates in units of cpsd and cpmsd. The 32 nHz estimation error corresponds to half the 64 nHz FFT frequency grid spacing. The fourth and fifth columns contain percentage relative differences between values in the first column and the values in the second and third columns, respectively (the denominators are the values from the first column). The fifth column contains multitaper standard deviation estimates for the peak frequencies. The last column contains multitaper Fisher statistic values.

$$\{1.0025, 1.9995, 3.0020, 3.9991, 5.0016, 7.9926\} \text{ cpsd}.$$

The fourth and fifth columns of Table 2 together reveal that frequency estimates for the rows associated with the $\mathbb{X}^{(HS)}$ harmonic components having the six listed frequencies above are systematically 2–11 times nearer to 1 cpsd harmonic frequencies than they are to 1 cpmsd harmonic frequencies. As anticipated by Little and Leinbach (1959), it appears that the cosmic HF emissions primarily explain the low frequency, high SNR content of the voltage process. That only six harmonic components are required to model the stable component of $\mathbb{x}^{(HS)}$ in quiet times might have been anticipated because sky maps of the Dominion Radio Astronomical Society (DRAO) Galactic Survey (see Figure 1 in Spanswick, 2005) effectively reveal a partitioning of the radio intensity into five distinct levels.

Table 2 also includes the statistics for $\mathbb{X}^{(MS)}$ harmonic components. Based on the frequency estimates, it is less clear whether the harmonic function frequencies systematically lie nearer to the 1 cpmsd or 1 cpsd harmonic frequencies. The medium SNR spectral peaks may well arise solely from the smoothing artifacts in the multitaper DFTs incurred by the record truncation that distinguishes $\mathbb{X}$ from $\mathbf{X}$.

4.2. The Detected Spectral Components of Low SNR

4.2.1. An Overview of the Spectral Content

For the OTT voltage series, the variance estimate for $X_n^{(RES)}$ is $4.9 \times 10^{-2}\text{V}^2$ (under 8% the estimated variance of $X_n^{(RES)}$). The variance estimate for $X_n^{(NL)}$ is $1.3 \times 10^{-3}\text{V}^2$ (under 3% the variance estimate for $X_n^{(RES)}$). These notable changes in scale highlight the importance of using spectral analysis when searching for low SNR signal elements because these might be hidden in a time domain analysis. For the other four CRA series, the variance scales of the model components are comparable. An increased variability of the INU and RES voltage series results in fewer significant peaks in their standardized spectra. As for the two ACE time series, it was found through visual inspection that the SWEPAM proton density series is more variable than each of the five CRA voltage series, culminating in notably fewer upcrossings of the 99% level of the standardized statistic spectrum than for the CRA standardized statistic spectra. The low sensitivity of the SWEPAM standardized statistic spectrum to spectral peaks is most apparent in Figure 3, which compares the SWEPAM and

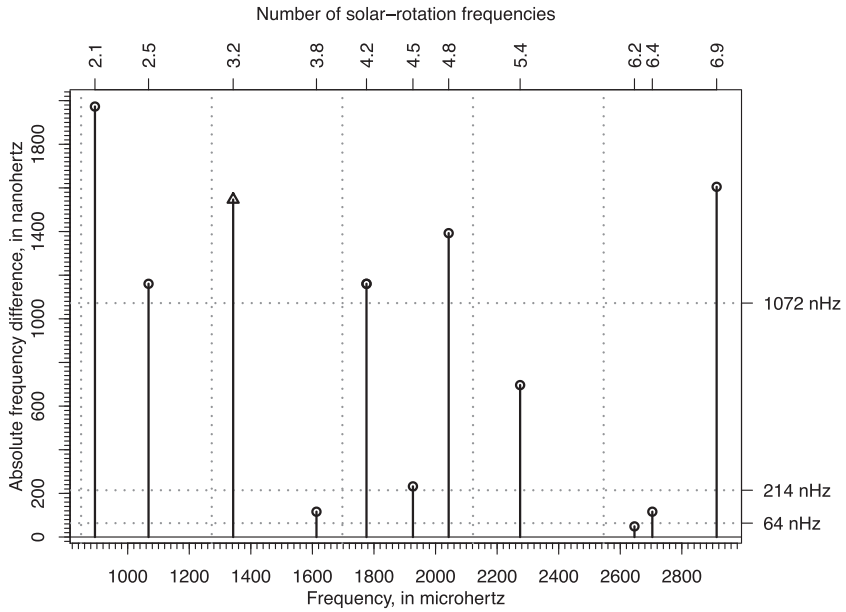

Figure 1. For the OTT voltage series described in Table 2, this plot displays the absolute differences between multiplet central frequency estimates and either 1 cpsd (circles) or 1 cpmsd (triangles) harmonic frequencies. Dashed, horizontal lines are drawn at the 64 nHz FFT grid spacing, the 214 nHz Rayleigh resolution, and the 1.072 μHz multitaper half bandwidth parameter. Dashed, vertical lines are drawn at the nearest solar rotation harmonic frequencies to abscissa of the plotted points.

OTT standardized spectra. While variability of the three IMF strength series is comparable with that of the proton density series, it was found through visual inspection that the IMF strength standardized spectrum typically has lower resolution bandwidth at the spectral peaks.

In the CRA standardized spectra, a number of 99.9% level multiplets appear whose splitting frequency is 1 cpsd. As will be seen in Figures 2 to 4, the multiplets can be identified by bands of the standardized spectrum that have the following characteristics.

1. Two or three singlet peaks rising above the 99.99% level of the standardized statistic spectrum.
2. A number of other peaks whose spectral power decays away from center on either side.
3. The spectral power decay profile is bell shaped.

The outstanding spectral peaks in the proton density standardized spectrum occur in the [2, 3] mHz frequency band. For example, four 99.9% level spectral peaks have narrow bandwidth on the scale of 10μHz, where the corresponding peak frequency estimates are $\{2.275, 2.704, 3.500, 3.775\}$mHz (with periods of $\{7.3, 6.2, 4.8, 4.4\}$ min, respectively).

4.2.2. Using Multiplets to Infer the Source Scale and Coupling Effects

In the detection scheme of section 2, Step A is to keep record of the narrow, >95% level spectral peaks found coincident in a number of CRA standardized spectra. This step led to the observation of nine outstanding multiplets in each of the OTT, BRD, and MEA standardized spectra, and these multiplets are summarized in Table 3. The table displays spectral power and multiplet central frequency estimates, along with the relevant frequency bands and the number of peaks. The current and following sections describe an underlying mechanism inferred from the frequency arrangement of these multiplets. All of the multiplet peaks have χ^2_{18} p values below 10^{-14}, so they are not spurious. With each multiplet consisting of six or more singlet peaks and decaying spectral power on either side of the central peak (see Figures 2 through 4 for examples), it is speculated that the six term signal element of section 4.1 drives periodic elements whose frequencies coincide with the multiplet central frequency estimates.

The following three examples regarding the Table 3 multiplets illustrate the value of Step A.

1. The recurrence of the nine multiplets in the OTT, BRD, and MEA standardized spectra suggests a modal source having either a continental or planetary scale.

Table 3
Summary Statistics for Multiplets in the Standardized Spectra of CRA Voltage Series Spanning the First 54 Days of 2011

Band (μHz)	Number of peaks	Central peak Frequency μHz	Central peak Frequency cpmsd	Central peak Frequency cpsd	Central peak Spectral power	CRA INU	CRA RES	ACE SWEPAM	ACE MAG
[859, 940]	8	888	76.7	76.5	9			1	1
[1,039, 1,097]	6	1,062	91.8	91.5	7		1		1
[1,306, 1,376]	7	1,330	114.9	114.6	9				1
[1,578, 1,636]	6	1,612	139.3	138.9	8				
[1,731, 1,801]	7	1,772	153.1	152.7	6			1	1
[1,899, 1,957]	6	1,923	166.1	165.7	6				1
[1,986, 2,056]	7	2,044	176.6	176.1	7				
[2,250, 2,320]	7	2,274	196.5	195.9	6	1		1	
[2,670, 2,752]	8	2,704	233.6	233.0	6	1		1	

Note. For the OTT, BRD, and MEA standardized spectra, each of the listed frequency bands contains a multiplet whose splitting frequency is 1 cpsd. The peak frequency and peak height estimates are provided for a singlet peak both achieving the maximum standardized statistic value in the multiplet and lying near the center of that multiplet. In the seventh and eighth columns, an entry value of "1" means that the INU and RES standardized spectra contain multiplets coincident with those of the OTT, BRD, and MEA standardized spectra. The final two columns are equivalent to the seventh and eighth columns, but now for the two ACE standardized spectra.

2. A sextuplet was detected in the [1.039, 1.097] mHz frequency band of the RES standardized spectrum (second row in Table 3). In isolation, the multiplet would be treated with suspicion because the singlet peaks achieve only 95% statistical significance. However, several of the singlet peaks are coincident with those of multiplets in the OTT, BRD, and MEA standardized spectra. Therefore, the RES multiplet substantiates the claim that the source has a continental or planetary scale.
3. Singlet peaks of the INU standardized spectrum in the [2.670, 2.752] mHz octuplet (ninth row in Table 3) resemble those of coincident multiplets in the OTT, BRD, and MEA standardized spectra. To a lesser extent, coincidences in the [2.250, 2.320] mHz frequency band of the INU standardized spectrum (eighth row in Table 3) suggest a common modal source.

4.2.3. A Physical Mechanism for the Multiplet Generation

Peak broadening, frequency drift, and statistical uncertainty all limit the extent to which individual spectral peaks explain the frequency arrangement of the nine multiplets of Table 3. By exploring the collective behavior of singlet peaks in a multiplet and the collective behavior between the nine multiplets themselves, it was found that these multiplets likely arise from a single external driver. The force function of this driver can be modeled by a Fourier series having the fundamental period, T_f, where $T_f \leq 12$ min. This conclusion has been reached because the presented evidence to follow suggests a coupling between the Fourier series terms and 1 cpsd harmonic components of the riometer voltage.

The 12 min upper bound was discovered from an exploration of the multiplets of Table 3 centered within 4μHz of the 1 cpsd harmonic frequencies. The first step was to establish that the multiplets behave as harmonics of a 1 cpsd Fourier series that additionally have been split by Earth's rotation. This result had been anticipated because peaks at 2.646 and 2.911 mHz (250.8 and 228.0 cpsd, respectively) had been detected at the 99.9% level of the multitaper harmonic Fisher statistic spectrum, confirming the presence of high order 1 cpsd subharmonics.

For the OTT voltage series, Figure 1 displays a spectrum of the absolute differences (solid, vertical lines) between a collection of frequency estimates based on the Table 3 entries and the nearest 1 cpsd (circles) and 1 cpmsd (triangles) harmonic frequencies (note that either a circle or a triangle is plotted at a given frequency because the circle or triangle not included exceeds 3μHz, well above the upper plotting bound). The following list specifies the frequency estimates included in the aforementioned collection.

1. Three point averages from the following Table 3 frequency estimates:
   - Central peak frequency estimates (third column).
   - Frequency estimates for both the leftmost and rightmost singlet peaks (first column).

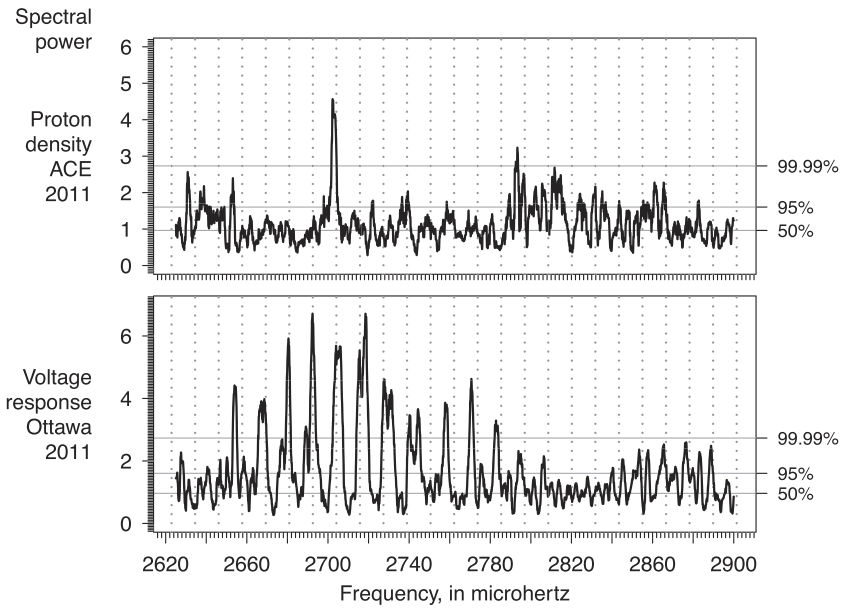

Figure 2. Standardized spectra for the SWEPAM proton mass density series (top plot) and the OTT voltage series (bottom plot). Both of the time series cover the first 54 days in 2011. The density has been measured for protons having energies in the [0.795, 1.193] MeV gate. Standardized spectrum estimates have each been divided by 18, the number of degrees of freedom of the χ^2_{18} distribution. Bold, gray, horizontal lines are drawn at one eighteenth the percentiles (labeled) of a χ^2_{18} distribution. The dotted, vertical lines are drawn at integer multiples of 1 cpsd.

Average estimates were used for multiplets listed in the following rows of Table 3: {1, 2, 4, 6, 8, 9}.
2. Central peak frequency estimates from the following rows of Table 3: {3, 5, 7}.
3. The frequency estimates, 2.646 and 2.911 mHz.

The top axis of Figure 1 displays multiples of the solar rotation harmonic frequency nearest the frequency estimates in the above collection. This is because the observation of spectral peaks near these rotation harmonic frequencies is precedented (e.g., refer to the relevant discussions in Thomson et al., 1997, 2007). The 27 day estimate for solar rotation period was used (Seidelmann, 1992; Thomson et al., 2007).

Figure 1 reveals a regular spacing between the frequency estimates in the above collection because of the consistent agreement of the estimates with the nearest 1 cpsd or 1 cpmsd harmonic frequencies to within 2μHz. Typically, the agreement is within the 1.072 μHz multitaper half bandwidth parameter, suggesting that the discrepancy could be linked to the smoothing effects of the record truncation distinguishing $\mathbb{X}$ from $\mathbf{X}$. Of the 11 plotted frequency differences, four lie below the 214 nHz FFT grid spacing in the case of no zero padding, while three of these differences lie below the 64 nHz grid spacing in the case of the zero padding given the rule of equation (D1). Often, the multiplet frequency estimates lie considerably further away from the solar rotation and 1 cpmsd harmonic frequencies than they do from the 1 cpsd harmonic frequencies. The hypothesis of the high order 1 cpsd harmonic components is further motivated by the fact that the 2.646 and 2.911 mHz estimates respectively lie within 64 nHz and 1.6μHz of a 1 cpsd harmonic frequency.

The following scheme resulted in the discovery of the T_f periodic element.

1. The frequency estimates were ordered by magnitude into a sequence.
2. The absolute differences between every one, every two, and every three sequence elements were computed, yielding three different sequences.
3. Period estimates associated with the differences in Step 2 were each divided by 12 min. Several of the resulting values were found to lie within two decimal places of an integer. Rounding these select 12 min multiples, the resulting values comprise a sequence that contains five unique integers: {2, 4, 5, 6, 9}.
4. The five element sequence of unique integers in Step 3 has unit greatest common divisor.

For each of the nine Table 3 multiplets, the absolute difference between the collection frequency estimate and at least one other collection estimate lies in the sequence of frequency differences considered in Step 3 of the above scheme.

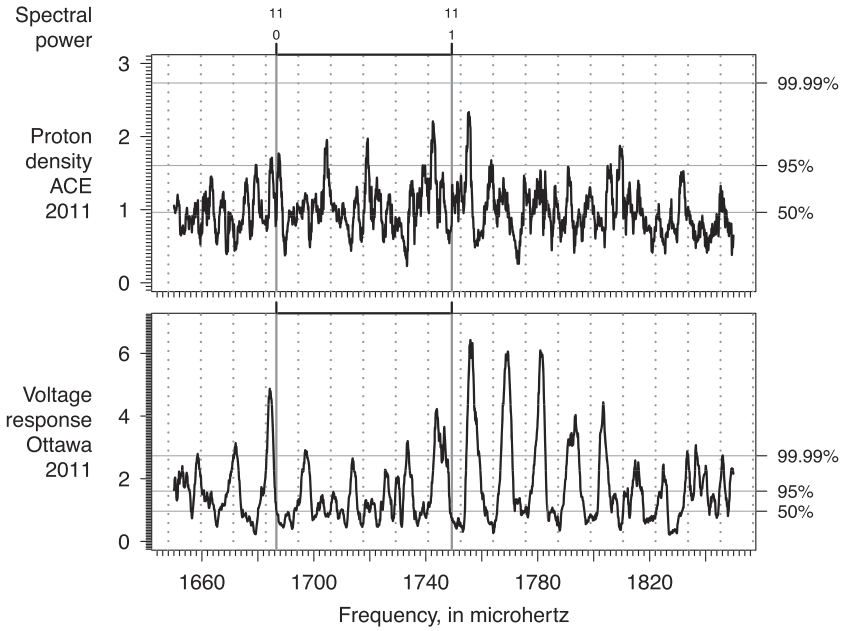

Figure 3. The same plots as in Figure 2, but now for the [1.650, 1.840] mHz frequency band. Bold, vertical, gray lines are drawn at reference p mode frequency estimates. For the labels in the top axis, the p mode radial order, n, is written above the latitudinal order, l. The remaining features are explained in Figure 2.

4.2.4. A 6 Min Driver for Signal Elements of Low SNR

In the detection scheme of Section 2, Step B is to keep record of those >95% level peaks in the two ACE standardized spectra found coincident with the peaks recorded in Step A. An implementation of Step B for the multiplet of the ninth row in Table 3 reveals a coupling between the riometer voltage and a 6 min periodic element, a result that provides some motivation for setting $T_f = 12$ min. Figure 2 displays the standardized spectra for both the OTT and SWEPAM time series as well as percentiles of the χ^2_{18} distribution. The most remarkable coincidence in the SWEPAM and OTT standardized spectra is a 2.704 mHz peak. The peak frequency corresponds to a 6.2 min periodic element, and it lies under 80μHz left of the 6 min mode frequency. In the SWEPAM standardized spectrum, the peak has a χ^2_{18} p value below 10^{-11}, making this peak the outstanding feature of that spectrum. In each of the OTT, BRD, and MEA standardized spectra, the 2.704 mHz peak appears centrally in one of the only Table 3 multiplets for which a multiplet in the INU standardized spectrum is coincident.

It is beyond the scope of this paper to propose a physical mechanism for the 6 min periodic element. The observation of a 6 min mode in space physics time series (Fehlau et al., 1971; Glencross, 1970) is precedented, although it is unclear whether there is a connection between the source of this periodic element and the 6 min periodic element identified in this paper.

4.2.5. A Coupling Between the Riometer Voltage and Specific Solar p Modes

This section presents two examples where an implementation of the mode detection scheme of section 2 reveals evidence for a coupling between the riometer voltage and solar p modes. The first example concerns the [1.650, 1.850]μHz band. Step C of the detection scheme in section 2 is to scan reference p mode frequency estimates, keeping a record of those which agree within 4μHz of the frequencies recorded in Steps A and B. The evidence suggests a coupling between the OTT riometer voltage and the $p_{11,1}$ mode. Figure 3 displays the same two standardized spectra as in Figure 2, but now for the [1.650, 1.840] mHz frequency band. At 1.749 mHz (where a solid, gray, vertical line has been drawn), it appears that the $p_{11,1}$ mode has coupled with both the SWEPAM proton density and the riometer voltage because spectral peaks of comparable width and power appear on either side of the $p_{11,1}$ reference frequency. The two singlet peaks are centered near 1.742 and 1.754 mHz (1 and 2μHz right of 150 and 151 cpsd, respectively). While it is possible that the two peaks in the SWEPAM standardized spectrum comprise a doublet, it is beyond the scope of this paper to speculate a plausible source for this splitting. Whatever the cause of these peaks, it does appear that the mode that induces the 1.754 mHz proton density peak also couples with the riometer voltage. A possible mechanism

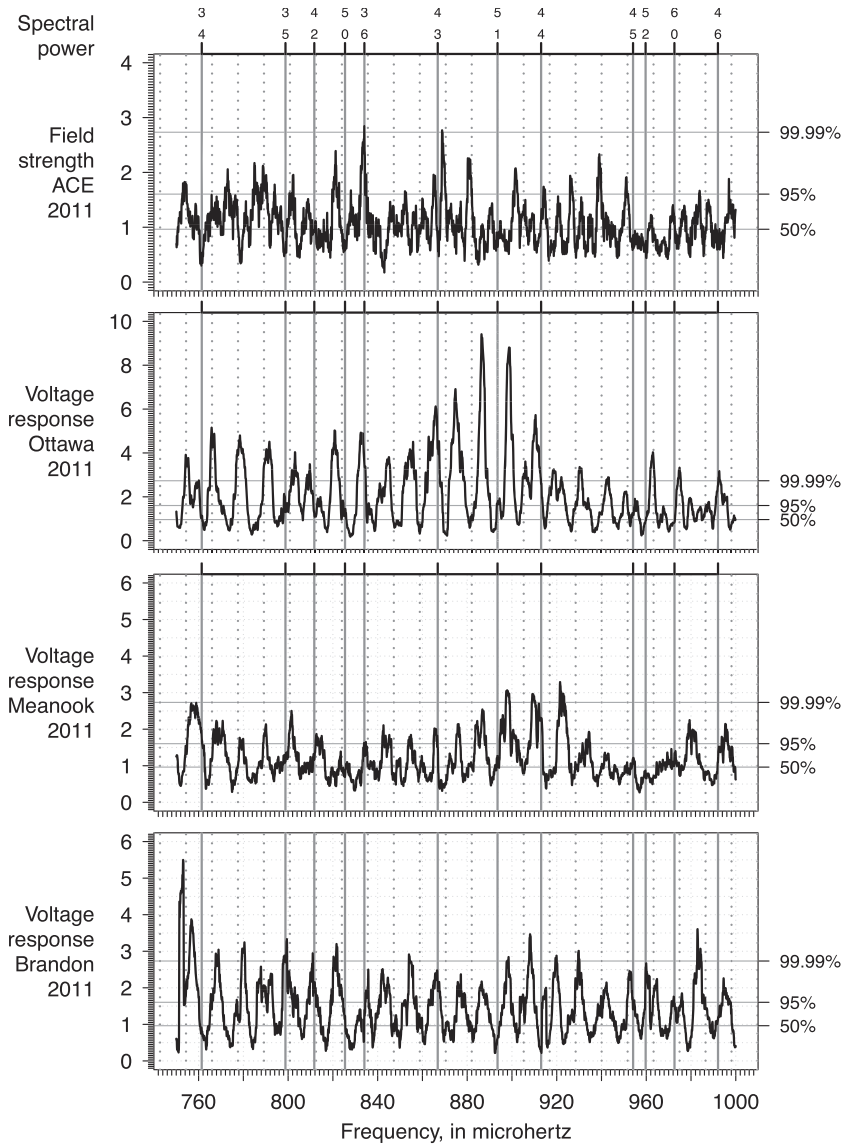

Figure 4. Standardized spectra for the MAG IMF strength series (top); the OTT voltage series (second from top); the MEA voltage series (third from top); and the BRD voltage series (bottom). For a description of the remaining features, refer to Figure 3.

for the peaks is that Earth's rotation splits the $p_{11,1}$ peak and then the two singlet modes couple with the modes inducing the two coincident peaks in the SWEPAM spectrum. Further evidence for the ACE OTT coupling events is a 95% level triplet in the MAG standardized spectrum (not depicted), which resembles the doublet of the SWEPAM standardized spectrum bar the addition of the central singlet peak at 1.749μHz.

Implementing Step D, reference p mode frequency estimates were scanned for the cases $n' = 11$ and $l' \neq 1$. Both of the standardized spectra in Figure 3 contain numerous peaks near the 1.687 mHz estimate for the $p_{11,0}$ mode (where a solid, gray, vertical line is drawn). Around the $[1.671, 1.696]$ mHz (144 to 146 cpsd) frequency band of the OTT standardized spectrum, a 99.9% level triplet is found centered on 1.684 mHz. The central singlet peak is coincident with a 95% level peak in the SWEPAM standardized spectrum. Given the 2 μHz uncertainty for frequency estimators discussed in section 3, 1.684 mHz agrees with 1.687 mHz. Unlike the case of the $p_{11,1}$ peaks, there are no significant coincidences in the SWEPAM standardized spectrum for the left and right singlet peaks, demonstrating that coincident peaks in the SWEPAM and OTT standardized spectra need not occur to ensure the 1 cpsd splitting for the voltage series.

After implementing Step E, the right 1.754 mHz peak of the 1.749 mHz SWEPAM doublet was found coincident with a peak in the 2004 seismic displacement standardized spectrum of Figure 4 in Thomson and Vernon (2015). The series was recorded at Black Forest Observatory (Landgraf, 2019), and the standardized spectrum was computed in a similar manner to that discussed in Appendix A for the standardized spectra in this paper. In the aforementioned reference figure, the missing 1.742 mHz left singlet peak could be due to the characteristic intermittency of solar modes (refer to p. 183 of Stix, 2004; Thomson, 1990). Thomson and Vernon (2015) suggest that the exceptional narrowness of the 1.754 mHz seismic peak (2 to 10 μHz bandwidth) limits the possible sources for these peaks to sources of high stability like those of solar origin.

The second example of p mode coupling involves coincidences in the ACE and CRA standardized spectra, which provide evidence for the $p_{5,1}$ mode. The top two plots in Figure 4 display the MAG and OTT standardized spectra in the [740, 980] μHz frequency band, while the bottom two plots display the corresponding BRD and MEA standardized spectra. For Step A, the octuplet in the OTT standardized spectrum (first row of Table 3) is centered on a frequency, which lies within 2μHz of the 894μHz (18.6 min) $p_{5,1}$ mode reference frequency estimate, while the lower two plots of Figure 4 reveal coincident multiplets in the BRD and MEA standardized spectra. Upon implementing Steps B and C, the 894 μHz OTT peak is coincident with a MAG peak. It also appears that the $p_{4,3}$ and $p_{4,4}$ modes couple with the riometer voltage. While the coincident IMF strength peaks each lie within 2μHz of singlet peaks of the 1 cpsd OTT, MEA, and BRD multiplets. This suggests that the disturbances at ACE also play a part in amplifying the singlet low SNR components of the riometer voltage. For Step D, all CRA standardized spectra in Figure 4 reveal a coupling between the $p_{4,4}$ mode and the riometer voltage due to peaks that are coincident with those in the MAG standardized spectrum. Meanwhile, a MAG peak 3μHz left of the $p_{5,0}$ frequency estimate is coincident with OTT and BRD peaks. Steps B–D also yield 95% level detections of coincident peaks in the MAG and CRA spectra of Figure 4, which all lie within 3μHz with the $p_{3,5}$ and $p_{3,6}$ frequency estimates.

5. Conclusions and Future Directions

The paper has presented three findings. The first is that the stable temporal behavior of riometer voltage is predominantly explained by a six term expansion in harmonic functions whose frequencies each lie near a 1 cpsd harmonic frequency.

The second finding is that the voltage of a CRA riometer interacts with the modes of physical phenomena other than just those associated with Earth's rotation. The evidence suggests that one of these phenomena is described by a Fourier series driver having 12 min fundamental period. Meanwhile, coincident peaks in the CRA and SWEPAM standardized spectra at 2.704mHz suggest that the spectral components of the riometer voltage are driven by an extraterrestrial force, which is periodic with 6 min period. The 800 μHz frequency difference associated with the detected 6 and 6.2 min periods implies that a relationship between the 6.2 min periodic and 12 min periodic elements remains suspect. However, the two periodic elements in question are the most prominent features in the spectral analysis of this paper, and it should be explored in a future analysis whether there is evidence to support the hypothesis of a relationship.

The third finding is that the riometer voltage couples with p modes previously observed in space physics data sets. The most convincing examples involve coincident peaks in the CRA and ACE standardized spectra whose frequency estimates agree with the reference estimates of p modes having the following labels: $p_{3,5}$, $p_{3,6}$, $p_{4,3}$, $p_{4,4}$, $p_{5,0}$, $p_{5,1}$, $p_{11,0}$, and $p_{11,1}$.

That there is strong evidence for mode transport in the geospace environment is indisputable, but specifying all of the sources that gave rise to the detected spectral peaks remains inconclusive solely based on the starting results of this paper. It remains to create a comprehensive list of the statistically significant spectral peaks in the CRA standardized spectra. In constructing this list, it is advisable to include information about the detected peaks that is obtained using a detection scheme similar to that of section 2. Source specification could be improved by scrutinizing the solar mode tables of Korzennik (2018). For further validation that solar modes couple with the riometer voltage, it would be beneficial to explore if coincidences exist in different seismic time series like those acquired by the USArrray Transportable Array (Vernon et al., 2012). Because of the preliminary nature of the analysis in this paper, the SWEPAM proton density time series at energy gates other than [0.795, 1.193] MeV should be analyzed in a follow up work.

Appendix A: A Statistical Detector for the Spectral Components of Low Signal to Noise Ratio

The statistical detector for the low signal to noise ratio (SNR) components of $\mathbb{X}$ in section 2 is based on the test statistic of equation (11) in Thomson et al. (2001). At the fast Fourier transform (FFT) frequency, f_m, this test statistic is equal to the scale, $2K$, of a ratio statistic. The numerator of this ratio statistic is that frequency f_m multitaper spectral power estimator for $\mathbb{X}^{(RES)}$, which is derived from the K frequency f_m multitaper DFT transformations of $\mathbf{X}$ after having subtracted from them the estimators of the mean associated with $\mathbb{X}^{(HS)}$ and $\mathbb{X}^{(MS)}$ (refer to the last equation preceding section XIV A of Thomson (1982) for the subtraction operation). The denominator of the ratio statistic is a product of the following two factors.

1. The frequency f_m value of a power transfer function (PTF) for the autoregressive (AR) filter relating $\mathbb{X}^{(RES)}$ and $\mathbb{X}^{(NL)}$.
2. A frequency f_m quantile spectral power estimator for $\mathbb{X}^{(PE)}$ (refer to Appendices C and D of Thomson et al., 2001).

The ratio statistic is an estimate for the scale, $2K$, of the test statistic in equation (7) in Thomson (2012). That statistic is also a ratio statistic, and its numerator is the frequency f_m multitaper spectral power estimator for $\mathbb{X}^{(NL)}$. The denominator of this ratio statistic is the expected value for the frequency f_m multitaper spectral power estimator for $\mathbb{X}^{(PE)}$. Under the null hypothesis that $x^{(LS,jh)} = 0$, the frequency $f^{(LS,jh)}$, standardized multitaper spectral power estimator is asymptotically distributed as a χ^2_{2K} random variable.

In the denominator of the standardized statistic, the AR filter coefficients were estimated using the methods in Appendix C of Thomson et al. (2001). The samples used in deriving the frequency f_m quantile spectral power estimator are multitaper spectral power estimators for $\mathbb{X}^{(NL)}$ in a 43 μHz frequency band (i.e., spanning 20 FFT frequencies). In particular, the quantile estimator itself is the 6% empirical quantile for this sample (refer to Appendix D in Thomson et al., 2001, for details of the method for selecting a suitable sample element).

Appendix B: Strengths and Weaknesses of the Detection Scheme for Spectral Components of Low Signal to Noise Ratio

The following remarks motivate the detection scheme of Section 2 for low signal to noise ratio (SNR) components.

Ⓐ Coincident peaks in the Canadian Riometer Array (CRA) standardized spectra suggest a single modal source having either a continental or planetary scale.

Ⓑ (a) To the extent that the multitaper DFTs are good estimates for the corresponding discrete time Fourier transforms, an invariance of the standardized statistic spectra to linear filter sequences obscures the true source of the spectral peaks recorded in Step A. For example, suppose that a periodic element is present either in the three interplanetary magnetic field (IMF) strengths measured at Magnetic Field Experiment (MAG) or in the chromospheric, Lyman alpha emissions discussed in section 1. If this periodic element was to couple with solar modes, then spectral peaks would appear in the CRA standardized spectra centered on the relevant resonant frequencies. Between them, the CRA standardized spectra alone would provide insufficient evidence to support the claim that the detected peaks are indeed of solar origin.

(b) The following references present evidence that the IMF strength couples with solar modes: Somerset (2017), Thomson et al. (1995), and Thomson et al. (2001). Magnetic fields of the SEPs perturb the IMF (Thomson et al., 2001), and so solar mode energy of the SEPs at ACE is transferred to the IMF. Therefore, periodicity of the SWEPAM proton mass density series might resemble that of the riometer voltage series.

Ⓒ A 4 to 8 μHz search bandwidth accounts for the dispersion attributed to damping, stochastic forcing, and estimation uncertainty (Thomson, 2000; Thomson & Vernon, 2015).

Ⓓ Suppose that a p mode with the angular momentum state, $|n, l, m\rangle$, couples with a spectral component of the voltage prediction error process, $\mathbb{X}^{(PE)}$. As long as the other $|n, l', m'\rangle$ states are locked

in phase, the corresponding low SNR components exhibit symmetry (Korzennik et al., 2013). It might thus be expected that these other singlet states also couple with spectral components of $\mathbb{X}^{(PE)}$.

Ⓔ Solar modes have frequency dependent lifetimes as low as a number of minutes and sometimes lasting up to a number of months (Chen et al., 1996). The solar convection zone generates new modes whose induced spectral peaks replace those that had been induced by the older modes that have decayed or vanished. If spectral peaks persist over years, then this is evidence for a stable source of modes like the Sun.

A limitation of the mode detection scheme is that some frequency bands of the $\mathbb{X}^{(NL)}$ power spectrum are densely packed with spectral peaks. The peaks in these frequency bands are smoothed due to the effects of record truncation of the time series model process, culminating in the formation of ridge spectral peaks (Korzennik et al., 2013). Ridge formation is common in the [2, 5] mHz frequency band in the spectrum of photospheric radial velocity because on average, there are 100 spectral peaks per microhertz (see Figure 11 of Christensen Dalsgaard, 2002). In anticipation of the degraded resolution quality, which comes with ridge formation, only the $|n, l, 0\rangle$ states of a p mode were considered in Steps C through E of the mode detection scheme.

Appendix C: The Correlation Between Solar Activity and p Mode Frequency Shifts

The shift of p mode frequencies over time is correlated with solar activity. For example, frequency shift is correlated with the Kitt Peak magnetic index and the He1 equivalent index (Chaplin et al., 2004). More pertinent to the results of this paper is the correlation between frequency shift and the 10.7 cm solar radio flux. This flux results from the emissions of bright, photospheric plasma regions overlying sunspots, as well as from chromospheric and coronal thermal emissions (Chaplin et al., 1998; Chaplin et al., 2001; Chaplin et al., 2004; Tapping, 2013; 2018). It has thus been speculated that the primary causes for the flux shift relationship are the spatiotemporal fluctuations occurring in solar magnetic field strength and in solar thermal variations (Balmforth et al., 1996; Chaplin et al., 2001; Goldreich et al., 1991; Gough et al., 1988; Thomson et al., 2007).

Appendix D: Calculations for the Multitaper Spectral Analysis

The riometer decimates 60 Hz voltage signals using an online, 60:1 median filter. Two point linear interpolation reconstructions were used to replace voltages either exceeding the 6.1 V instrument ceiling or occurring during hourly, 1 min calibration intervals. The two points for each interpolation were 10 point averages on either side of the gap of omitted voltage outliers. At calibration intervals, the updating step of Appendix A in Thomson et al. (2001) was employed. In this step, the training set was chosen to comprise two 120 point sections on either side of the 60 point calibration interval. In addition, the multitaper time bandwidth parameter was set equal to 3 because a low resolution bandwidth is desirable for short time records (Thomson et al., 2001). Furthermore, the number of tapers was set equal to 5. Each of the cleaned CRA voltage series was sent through a 120:1 decimation filter whose associated PTF has a transition band commencing at (4 mHz; 50 dB) and decaying at 0.5 dB/mHz.

But for the following two exceptions, the aforementioned processing steps for the CRA voltage series were also carried out for the two 1 min sampled ACE time series.

1. Neither of the two 1 min sampled time series required cleaning.
2. Both of the time series were decimated using sequential two point averaging.

For each of the considered time series of this paper, the record size, M, after zero padding was set using the rule,

$$\log_2(M) = \lfloor \log_2(N) + 1 \rfloor, \tag{D1}$$

where $N = 3.8863 \times 10^4$ defines the record size of each of the CRA voltage series. Defining M this way reduces the roundoff error and the FFT computation time (Gentleman, 1969), while yielding a common FFT grid of 64 nHz spacing for all of the considered time series. Following the procedure outlined in Appendix C of Thomson et al. (2001), AR PTF sequences having the orders, $P \in \{1, 2, ..., 10\}$, were estimated by first

computing an inverse FFT of the multitaper power spectrum estimate for the OTT voltage series and then implementing the Durbin Levinson algorithm using the resulting autocovariance sequence estimate. The multitaper dynamic range estimate is the ratio of maximum to minimum estimated spectral power, and it is measured in decibels (Percival & Walden, 1998). The AR PTF sequence estimate was obtained using the set of coefficient estimates for the p value achieving minimum dynamic range (e.g., $p = 3$ was optimal for the OTT voltage series). The AR PTFs were computed analogously for the remainder of the considered time series.

As in Appendix C of Thomson et al. (2001), a second whitening step was applied to estimate the power spectrum of $\mathbb{X}^{(PE)}$ (refer to Appendix A). In this whitening step, the FFT frequency grid was partitioned into sections of 43 μHz width. The ordered spectral power estimates of each section were used to compute a single quantile spectral power estimate for $\mathbb{X}^{(PE)}$ to estimate the power for each section frequency. Choosing the band sample associated with the 6% empirical section quantile ensures that the resulting spectral power estimator is optimal in a mean square sense (see Appendix D of Thomson et al., 2001). Choosing a section width below 43μHz reduces the effective number of independent band samples from the 34 such samples achieved originally. Meanwhile, it was found through experimentation that a section width exceeding 43μHz covers a frequency band whose spectral power estimates exhibit a significant degree of nonstationarity over frequency, so that the constant power approximation for

Acronyms

ACE	Advanced Composition Explorer
AR	autoregressive
BRD	Brandon
cpmsd	cycles per mean solar day
cpsd	cycles per sidereal day
CRA	Canadian Riometer Array
CSWFC	Canadian Space Weather Forecast Centre
DFT	discrete Fourier transform
DRAO	Dominion Radio Astronomical Observatory
FFT	fast Fourier transform
HF	high frequency
HS	high signal to noise ratio
IMF	interplanetary magnetic field
INU	Inuvik
LIN	linear
LS	low signal to noise ratio
MAG	Magnetic Field Experiment
MEA	Meanook
MS	medium signal to noise ratio
m.s.	mean square
OTT	Ottawa
NL	nonlinear
PE	prediction error
PEN	penticton
PTF	power transfer function
NL	power transfer function
RES	residual
Riometer	relative ionospheric opacity meter
SAS	Saskatoon
SEP	solar energetic proton
SFU	solar flux unit
SNR	signal to noise ratio
SWEPAM	Solar Wind Electron Proton Alpha Monitor

Acknowledgments
"Marshall_Francois_Supporting _Information_JGR_2019.pdf" contains a summary of the supporting information. The 1 hr sampled F10.7 series was obtained from DRAO (National Research Council, 2017). The three MAG time series of IMF strength were acquired from The ACE Science Center (2007), while the SWEPAM time series of proton mass density was acquired from Space Weather Prediction Center, National Oceanic and Atmospheric Administration (2018). The relevant data sets for the analysis of this paper are included in Marshall (2019). This work was supported by the Natural Sciences and Engineering Research Council of Canada (NSERC), Canadian Statistical Sciences Institute (CANSSI), Bonneyville Power Authority, and Queen's University. David J. Thomson, the official holder of the grants and contracts, provided research and conference funding to advance this project. Special thanks to Ken F. Tapping (DRAO of NRCan) for his guidance in finding the data sets relevant to solar radio emissions. Glen Takahara, of the Department of Mathematics and Statistics at Queen's University, suggested exploring different data sets to confirm the modal origin of spectral peaks observed in the Ottawa riometer of the CRA. Alessandra A. Pacini of the Arecibo Observatory recommended checking to see if some of the modes could have been driven by the harmonics of Earth's rotation. Frank Vernon of the Institute of Geophysics and Planetary Physics at Scripps Institution of Oceanography confirmed how seismic data could be expected to reveal coincident spectral peaks at the detected frequencies in the riometer standardized spectra.

References

ACE/MAG Project (2008). https://www.ssg.sr.unh.edu/mag/ACE.html (University of New Hampshire Experimental Space Plasma Group, Accessed 2019-07-06, Last updated 2008-10-21).

Agnew, D. C. (2019). An improbable observation of the diurnal core resonance. *Geodynamics and Earth tides observations from global to micro scale* (pp. 5–15): Springer.

Andrews, D. W. K. (1983). First order autoregressive processes and strong mixing (*664*): Cowles Foundation for Research in Economics, Yale University. https://cowles.yale.edu/sites/default/files/files/pub/d06/d0664.pdf

Baker, G. J., Donovan, E. F., & Jackel, B. J. (2003). A comprehensive survey of auroral latitude Pc5 pulsation characteristics. *Journal of Geophysical Research*, *108*(A10), 1384. https://doi.org/10.1029/2002JA009801

Balmforth, N. J., Gough, D. O., & Merryfield, W. J. (1996). Structural changes to the Sun through the solar cycle. *Monthly Notices of the Royal Astronomical Society*, *278*(2), 437–448. https://doi.org/10.1093/mnras/278.2.437

Berthomieu, G., & Provost, J. (1991). The asymptotic spectrum of gravity modes as a function of the solar structure standard solar model. *Solar Physics*, *133*, 127–138. https://doi.org/10.1007/BF00149833

Brillinger, D. R. (1981). *Time series: Data analysis and theory*, vol. 36: Siam.

Brockwell, P. J., & Davis, R. A. (1991). *Time series: Theory and methods*. Springer Science & Business Media.

Brockwell, P. J., & Davis, R. A. (2002). *Introduction to time series and forecasting* (Vol. 2). Springer.

Broomhall, A. M., Chaplin, W. J., Davies, G. R., Elsworth, Y., Fletcher, S. T., Hale, S. J., et al. (2009). Definitive Sun as a star p mode frequencies: 23 years of BiSON observations. *Monthly Notices of the Royal Astronomical Society: Letters*, *396*(1), L100–L104. https://doi.org/10.1111/j.1745-3933.2009.00672.x, .

Browne, S., Hargreaves, J. K., & Honary, B. (1995). An imaging riometer for ionospheric studies. *Electronics & Communication Engineering Journal*, *7*(5), 209–217. https://doi.org/10.1049/ecej:19950505, .

Burr, W. S. (2012). Air pollution and health: Time series tools and analysis (Ph.D. Thesis), Queen's University.

Buttighoffer, A., Lanzerotti, L. J., Thomson, D. J., Maclennan, C. G., & Forsyth, R. J. (1999). Spectral analysis of the magnetic field inside particle propagation channels detected by ULYSSES. *Astronomy and Astrophysics*, *351*, 385–392.

Chaplin, W. J., Elsworth, Y., Isaak, G. R., Lines, R., McLeod, C. P., Miller, B. A., & New, R. (1998). Solar p mode excitation: Further insight from recent low *l* BiSON helioseismological data. *Monthly Notices of the Royal Astronomical Society*, *298*(1), L7–L11. https://doi.org/10.1046/j.1365-8711.1998.01800.x

Chaplin, W. J., Elsworth, Y., Isaak, G. R., Marchenkov, K. I., Miller, B. A., & New, R. (2001). Changes to low *l* solar p mode frequencies over the solar cycle: Correlations on different time scales. *Monthly Notices of the Royal Astronomical Society*, *322*(1), 22–30. https://doi.org/10.1046/j.1365-8711.2001.04098.x, .

Chaplin, W. J., Elsworth, Y., Isaak, G. R., Miller, B. A., & New, R. (2004). The solar cycle as seen by low *l* p mode frequencies: Comparison with global and decomposed activity proxies. *Monthly Notices of the Royal Astronomical Society*, *352*(4), 1102–1108. https://doi.org/10.1111/j.1365-2966.2004.07998.x

Chave, A. D., Luther, D. S., & Thomson, D. J. (2019). High *Q* spectral peaks and nonstationarity in the deep ocean infragravity wave band: Tidal harmonics and solar normal modes. *Journal of Geophysical Research: Oceans*, *124*, 2072–2087. https://doi.org/10.1029/2018JC014586

Chave, A. D., Thomson, D. J., & Luther, D. S. (2018a). Quantifying the nonstationarity, nonlinearity and non Gaussianity of geomagnetic field variations over 400–4000 microHz, Washington, DC.

Chave, A. D., Thomson, D. J., & Luther, D. S. (2018b). *Why do EM data pervasively follow a stable distribution?* Helsingør, Denmark: 24th EM Induction Workshop.

Chen, K. R., Chou, D. Y., & Team, T. (1996). Determination of the lifetime of high *l* solar p modes from the interaction of p mode waves with sunspots. *The Astrophysical Journal*, *465*, 985–993. https://doi.org/10.1086/177484

Christensen Dalsgaard, J. (2002). Helioseismology. *Reviews of Modern Physics*, *74*, 1073–1129. https://doi.org/10.1103/RevModPhys.74.1073

Claverie, A., Isaak, G. R., McLeod, C. P., Van der Raay, H. B., & Cortes, T. R. (1979). Solar structure from global studies of the 5 minute oscillation. *Nature*, *282*(5739), 591.

Danskin, D. W., Boteler, D., Donovan, E., & Spanswick, E. (2008). The Canadian Riometer Array. In *Proceedings of the 12th International Ionospheric Effects Symposium*, Alexandria, VA, USA, pp. 80–86.

de Groot Hedlin, C. D. (2016). Long range propagation of nonlinear infrasound waves through an absorbing atmosphere. *The Journal of the Acoustical Society of America*, *139*(4), 1565–1577. https://doi.org/10.1121/1.4944759

de Pontieu, B., Erdélyi, R., & De Moortel, I. (2005). How to channel photospheric oscillations into the corona. *The Astrophysical Journal Letters*, *624*(1), L61. https://doi.org/10.1086/430345

Deubner, F L. (2002). *Solar neutrinos: The first thirty years*. In Bahcall, J. N., R. Davis Jr., P. Parker, A. Smirnov, & R. Ulrich (Eds.) (pp. 402–406). CRC Press.

Edgar, J. S. (2018). *Observer's handbook 2018*. In J. S. Edgar (Eds.). Toronto: Royal Astronomical Society of Canada.

Erdélyi, R. (2005). Magnetic coupling of waves and oscillations in the lower solar atmosphere: Can the tail wag the dog? *Philosophical Transactions of the Royal Society A: Mathematical, Physical and Engineering Sciences*, *364*(1839), 351–381. https://doi.org/10.1098/rsta.2005.1703

Fehlau, P. E., Chambers, W. H., Fuller, J. C., Kunz, W. E., Milkey, R. W., & Blocker, N. K. (1971). Periodic solar flare X ray emission. *Nature*, *232*(5305), 42. https://doi.org/10.1038/232042a0

Fiori, R. A. D., & Danskin, D. W. (2016). Examination of the relationship between riometer derived absorption and the integral proton flux in the context of modeling polar cap absorption. *Space Weather*, *14*, 1032–1052. https://doi.org/10.1002/2016SW001461

Fisher, R. A. (1939). The comparison of samples with possibly unequal variances. *Annals of Eugenics*, *9*(2), 174–180. https://doi.org/10.1111/j.1469-1809.1939.tb02205.x

Fisk, L. A. (1995). Exploring the heliosphere in three dimensions a keynote presentation. *Space Science Reviews*, *72*(1 2), 5–13.

Fisk, L. A. (1996). Motion of the footpoints of heliospheric magnetic field lines at the Sun: Implications for recurrent energetic particle events at high heliographic latitudes. *Journal of Geophysical Research*, *101*(A7), 15,547–15,553. https://doi.org/10.1029/96JA01005

Foppiano, A. J., & Bradley, P. A. (1985). Morphology of background auroral absorption. *Journal of Atmospheric and Terrestrial Physics*, *47*(7), 663–674. https://doi.org/10.1016/0021-9169(84)90130-2

Gentleman, W. M. (1969). An error analysis of Goertzel's (Watt's) method for computing Fourier coefficients. *The Computer Journal*, *12*(2), 160–164. https://doi.org/10.1093/comjnl/12.2.160

Ghosh, S., Thomson, D. J., Matthaeus, W. H., & Lanzerotti, L. J. (2009). Coexistence of turbulence and discrete modes in the solar wind. *Journal of Geophysical Research*, *114*, A08106. https://doi.org/10.1029/2009JA014092

Glencross, W. M. (1970). Six minute periodicity during X ray flares. *Nature*, *228*(5272), 654. https://doi.org/10.1038/228654a0
Goldreich, P., Murray, N., Willette, G., & Kumar, P. (1991). Implications of solar p mode frequency shifts. *Astrophysical Journal*, *370*(2), 752–762.
Gough, D. (1980). Some theoretical remarks on solar oscillations, *Nonradial and nonlinear stellar pulsation*. https://doi.org/10.1007/3-540-09994-8_27
Gough, D. O., Thompson, M. J., Christensen Dalsgaard, J., & Frandsen, S. (1988). Advances in helio and asteroseismology. In *Proc. IAU Symp*, *123*, pp. 175.
Gough, D., & Toomre, J. (1992). Instructions for the two dimensional hounds (*19*): Global Oscillations Network Group, National Optical Astronomy Observatories. Technical Report 11.
Granger, C. W. J. (1976). Tendency towards normality of linear combinations of random variables. *Metrika*, *23*(1), 237–248. https://doi.org/10.1007/BF01902870
Haley, C. L. (2014). Nonparametric and parametric methods for solar oscillation spectra (Ph.D. Thesis), Queen's University.
Hannan, E. (1970). *Multiple time series*. New York.
Hargreaves, J. K. (2010). Auroral radio absorption: The prediction question. *Advances in Space Research*, *45*(9), 1075–1092. https://doi.org/10.1016/j.asr.2009.10.026
Hill, H. A., Stebbins, R. T., & Oleson, J. R. (1975). The finite Fourier transform definition of an edge on the solar disk. *The Astrophysical Journal*, *200*, 484–498.
Isserstedt, J., & Schlosser, W. (1975). Intensitätsfluktuationen im kopf des kometen 1973f. *Astronomy & Astrophysics*, *41*, 9–13.
Jansky, K. G. (1933). Electrical disturbances apparently of extraterrestrial origin. *Proceedings of the Institute of Radio Engineers*, *21*(10), 1387–1398. https://doi.org/10.1109/JRPROC.1933.227458
Kim, H., Soto chavez, A. R., Takahashi, K., Adewuyi, M., Gerrard, A. J., Lanzerotti, L. J., et al. (2018). *Van Allen Probes observations of symmetric, compressional ULF waves in association with interplanetary shocks*. Washington, DC.
Korzennik, S. G. (2018). Medium l table. https://www.cfa.harvard.edu/~sylvain/research/tables/MediumL/MDI/01e.jsBo=0/Accessed: 2018 12 04.
Korzennik, S. G., Rabello Soares, M. C., Schou, J., & Larson, T. P. (2013). Accurate characterization of high degree modes using MDI observations. *Journal of Physics*, *772*, 87. https://doi.org/10.1088/1742-6596/440/1/012016
Kosovichev, A. G., Schou, J., Scherrer, P. H., Bogart, R. S., Bush, R. I., Hoeksema, J. T., et al. (1997). Structure and rotation of the solar interior: Initial results from the MDI medium l program, *The first results from SOHO* (pp. 43–61). Springer.
Laštovička, J (1976). The dependence of the ionospheric absorption at 2775 kHz on the intensity of ionizing radiation: Ionospheric implications. *Pure and Applied Geophysics*, *114*(3), 321–331.
Landgraf, S. (2019). Black Forest Observatory (BFO). https://www.gik.kit.edu/black_forest_observatory.phpKIT GIK Forschung, Accessed: 2019 10 23, Last updated 2019.
Little, C. G., & Leinbach, H. (1959). The riometer—A device for the continuous measurement of ionospheric absorption. *Proceedings of the IRE*, *47*(2), 315–320. https://doi.org/10.1109/JRPROC.1959.287299
Loève, M. (1960). *Probability theory, the university series in higher mathematics*. Princeton, NJ Toronto New York London: D. Van Nostrand Co., Inc.
Mallows, C. (1967). Linear processes are nearly Gaussian. *Journal of Applied Probability*, *4*(2), 313–329. https://doi.org/10.2307/3212026
Marshall, F. A. (2019). Spectral analysis of voltage data taken from the Canadian Riometer Array. https://catalogue.ceda.ac.uk/uuid/a119b841548c4948b2711f2ddbbe2e27,_Lastupdated2019,_Viewed2019
Marshall, F. A., Takahara, G., & Thomson, D. J. (2018). A multitaper test for the detection of non stationary processes using canonical correlation analysis. In *2018 IEEE Statistical Signal Processing Workshop (SSP)*, pp. 702–706. https://doi.org/10.1109/SSP.2018.8450806
Marshall, F. A., & Thomson, D. J. (2017). Robust mode detection schemes in a non stationary environment. In *JSM Proceedings, Section on Physical and Engineering Sciences*, Alexandria, VA, USA.
National Research Council (2017). Daily flux values for the year 2011. https://www.spaceweather.gc.ca/solarflux/sx-5-flux-en.php?year=2011,_Lastupdated2017;Accessed12/12/17
Natural Resources Canada (2019). HF radio propagation.
NOAA (2018). DRAO noontime flux. https://www.ngdc.noaa.gov/stp/space-weather/solar-data/solar-features/solar-radio/noontime-flux/penticton/penticton_observed/listings/drao_noontime-flux-observed_daily.txt (NOAA Solar-terrestrial Physics) .
Percival, D. B., & Walden, A. T. (1998). *Spectral analysis for physical applications: Multitaper and conventional univariate techniques*: Cambridge University Press.
Prölss, G. W. (2010). *Physics of the Earth's space environment: An introduction*: Springer.
Provost, J., Berthomieu, G., & Morel, P. (2000). Low frequency p and g mode solar oscillations. *Astronomy and Astrophysics*, *353*, 775–785.
Rahim, K., & Burr, W. S. (2017). Package "multitaper". https://cran.r-project.org/web/packages/multitaper/multitaper.pdf
Rogers, N. C., & Honary, F. (2015). Assimilation of real time riometer measurements into models of 30 MHz polar cap absorption. *Journal of Space Weather and Space Climate*, *5*, A8. https://doi.org/10.1051/swsc/2015009
Rosenblatt, M. (1961). Some comments on narrow band pass filters. *Quarterly of Applied Mathematics*, *18*(4), 387–393.
Schwenn, R. (2007). Solar wind sources and their variations over the solar cycle, *Solar dynamics and its effects on the heliosphere and Earth* (pp. 51–76). Springer.
Seidelmann, P. K. (1992). *Explanatory supplement to the astronomical almanac*: University Science Books.
Smith, C. W., & L'Heureux, J. (2003). Solar Wind Electron Proton Alpha Monitor (SWEPAM) for the Advanced Composition Explorer. https://swepam.lanl.gov,_Lastupdated2003,_Viewed2018
Snedecor, G. W. (1938). Statistical methods. xiii, 388, 388 (xii).
Somerset, E. (2017). Multitaper methods for cyclostationary feature detection in time series data: Application to ACE interplanetary magnetic field data (Ph.D. Thesis), Queen's University.
Space Weather Prediction Center, National Oceanic and Atmospheric Administration (2018). ACE real time solar wind. https://www.swpc.noaa.gov/products/ace-real-time-solar-wind,_Accessed:2018-12-04
Spanswick, E. (2005). Canopus quiet day curve generation. NORSTAR, University of Calgary, https://aurora.phys.ucalgary.ca/norstar/rio/doc/CANOPUS_Riometer_Baselining.pdf,_Lastupdated2005;Accessed06/12/2017
Spanswick, E., Donovan, E., Liu, W., Liang, J., Blake, J. B., Reeves, G., et al. (2009). Global observations of substorm injection region evolution: 27 August 2001. *Annals of Geophysics*, *27*(5), 2019–2025.
Steffens, S., & Nuernberger, D. (1998). Probing 5 minute oscillations in the solar wind with comet Hale Bopp (C/1995 O1). *Astronomy and Astrophysics*, *336*, 769–775.

Stein, R. F., & Leibacher, J. (1974). Waves in the solar atmosphere. *Annual Review of Astronomy and Astrophysics*, *12*(1), 407–435. https://doi.org/10.1146/annurev.aa.12.090174.002203
Stix, M. (2004). *The Sun: An introduction*. Springer.
Tapping, K. F. (2013). The 10.7 cm solar radio flux ($F_{10.7}$). *Space Weather*, *11*, 394–406. https://doi.org/10.1002/swe.20064
Tapping, K. (2018). *Observer's handbook 2018*. In J. S. Edgar (Ed.). Toronto: Royal Astronomical Society of Canada.
Tassoul, M. (1980). Asymptotic approximations for stellar nonradial pulsations. *The Astrophysical Journal Supplement Series*, *43*, 469–490. https://doi.org/10.1086/190678
The ACE Science Center (2007). About MAG data. https://www.srl.caltech.edu/ACE/ASC/level2/mag_l2desc.html(The ACE Science Center, Accessed: 2019 07 06, Last updated 2007 11 07)
Thompson, M. J. (2005). Magnetohelioseismology. *Philosophical Transactions of the Royal Society A: Mathematical, Physical and Engineering Sciences*, *364*(1839), 297–311. https://doi.org/10.1098/rsta.2005.1700
Thomson, D. J. (1982). Spectrum estimation and harmonic analysis. *Proceedings of the IEEE*, *70*(9), 1055–1096. https://doi.org/10.1109/PROC.1982.12433
Thomson, D. J. (1990). Quadratic inverse spectrum estimates: Applications to palaeoclimatology. *Philosophical Transactions of the Royal Society of London*, *332*(1627), 539–597. https://doi.org/10.1098/rsta.1990.0130
Thomson, D. J. (1990). Time series analysis of Holocene climate data. *Philosophical Transactions of the Royal Society of London. Series A, Mathematical and Physical Sciences*, *330*(1615), 601–616. https://doi.org/10.1098/rsta.1990.0041
Thomson, D. J. (2000). *Nonlinear and nonstationary signal processing Edited by* Fitzgerald, W. J., Smith, R. L., Walden, A. T., & Young, P. C., pp. 317–394, London, UK: Cambridge Univ. Press.
Thomson, D. J. (2007). Jackknifing multitaper spectrum estimates. *IEEE Signal Processing Magazine*, *24*(4), 20–30. https://doi.org/10.1109/MSP.2007.4286561
Thomson, D. J. (2012). *Background magnetospheric variability as inferred from long time series of GOES data*, pp. 225–241, AGU. https://doi.org/10.1029/2012GM001318
Thomson, D. J., & Chave, A. D. (1991). *Advances in spectrum analysis and array processing*. In S. S. Haykin (Ed.), pp. 58–113. Prentice Hall.
Thomson, D. J., & Haley, C. L. (2014). Spacing and shape of random peaks in non parametric spectrum estimates. *Proceedings of the Royal Society A: Mathematical, Physical and Engineering Sciences*, *470*(2167). https://doi.org/10.1098/rspa.2014.0101
Thomson, D. J., Lanzerotti, L. J., & Maclennan, C. G. (2000). Coherent frequency variations in electron fluxes at 1 and 5 AU in the inner heliosphere. In *AIP Conference Proceedings*, *528*, AIP, pp. 278–281. https://doi.org/10.1063/1.1324325
Thomson, D. J., Lanzerotti, L. J., & Maclennan, C. G. (2001). Interplanetary magnetic field: Statistical properties and discrete modes. *Journal of Geophysical Research*, *106*(A8), 15,941–15,962. https://doi.org/10.1029/2000JA000113
Thomson, D. J., Lanzerotti, L. J., Maclennan, C. G., Heber, B., Kunow, H., & Gold, R. E. (2001). Coherence of charged particle oscillations in the heliosphere ($f \approx 5\mu$Hz): Implications for a solar modulation source. *Journal of Geophysical Research*, *106*(A12), 29,341–29,354. https://doi.org/10.1029/2001JA000011
Thomson, D. J., Lanzerotti, L. J., Vernon, F. L., Lessard, M. R., & Smith, L. T. P. (2007). Solar modal structure of the engineering environment. *Proceedings of the IEEE*, *95*(5), 1085–1132. https://doi.org/10.1109/JPROC.2007.894712
Thomson, D. J., Maclennan, C. G., & Lanzerotti, L. J. (1995). Propagation of solar oscillations through the interplanetary medium. *Nature*, *376*, 139–144. https://doi.org/10.1038/376139a0
Thomson, D. J., Maclennan, C. G., & Lanzerotti, L. J. (1997). Recurrences of interplanetary interaction regions at southern solar latitudes and approximate harmonics. *Advances in Space Research*, *20*(1), 103–106. https://doi.org/10.1016/S0273-1177(97)00489-4
Thomson, D. J., & Vernon, F. L. (2015). Unexpected, high *Q*, low frequency peaks in seismic spectra. *Geophysical Journal International*, *202*(3), 1690–1710. https://doi.org/10.1093/gji/ggv175
Thornton, S., & Marion, J. B. (2004). Classical dynamics of particles and systems. *Brooks Cole, New York*.
Ulrich, R. K., & Rhodes Jr. E. J. (1977). The sensitivity of nonradial p mode eigenfrequencies to solar envelope structure. *The Astrophysical Journal*, *218*, 521–529.
Vernon, F., Tytell, J., Busby, B., Eakins, J., Hedlin, M., Muschinski, A., et al. (2012). Scientific viability of the USArray Transportable Array Network as a real time weather monitoring platform. In *2nd American Meteorological Society Annual Meeting*.